On the Along-Slope Heat Loss of the Boundary Current in the Eastern Arctic Ocean

Schulz, Kristin; Janout, M.A.; Lenn, Yueng-Djern; Castillo, Eugenio Ruiz ; Polyakov, Igor ; Mohrholz, Volker ; Tippenhauer, Sandra; Reeve, Krissy; Holemann, Jens; Rabe, Bemjamin; Vredenborg, Myriel

Journal of Geophysical Research: Oceans

[Cyswllt i'r cyhoeddiad / Link to publication](#)

19. Apr. 2024

Correspondence to:
K. Schulz,
kirstin.schulz@awi.de

On the Along-Slope Heat Loss of the Boundary Current in the Eastern Arctic Ocean

Kirstin Schulz[1] [ID], **Markus Janout**[1] [ID], **Yueng-Djern Lenn**[2] [ID], **Eugenio Ruiz-Castillo**[1] [ID], **Igor Polyakov**[3] [ID], **Volker Mohrholz**[4] [ID], **Sandra Tippenhauer**[1] [ID], **Krissy Anne Reeve**[1] [ID], **Jens Hölemann**[1] [ID], **Benjamin Rabe**[1] [ID], and **Myriel Vredenborg**[1] [ID]

[1]Alfred-Wegener-Institut Helmholtz-Zentrum für Polar- und Meeresforschung, Bremerhaven, Germany, [2]School of Ocean Sciences, Bangor University, Menai Bridge, UK, [3]International Arctic Research Center, College of Natural Science and Mathematics, University of Alaska Fairbanks, Fairbanks, USA, [4]Leibniz Institute for Baltic Sea Research, Rostock, Germany

Abstract This study presents recent observations to quantify oceanic heat fluxes along the continental slope of the Eurasian part of the Arctic Ocean, in order to understand the dominant processes leading to the observed along-track heat loss of the Arctic Boundary Current (ABC). We investigate the fate of warm Atlantic Water (AW) along the Arctic Ocean continental margin of the Siberian Seas based on 11 cross-slope conductivity, temperature, depth transects and direct heat flux estimates from microstructure profiles obtained in summer 2018. The ABC loses on average $\mathcal{O}(10^8)$ J m^{-2} per 100 km during its propagation along the Siberian shelves, corresponding to an average heat flux of 47 W m^{-2} out of the AW layer. The measured vertical heat flux on the upper AW interface of on average 10 W m^{-2} in the deep basin, and 3.7 W m^{-2} above the continental slope is larger than previously reported values. Still, these heat fluxes explain less than 20% of the observed heat loss within the boundary current. Heat fluxes are significantly increased in the turbulent near-bottom layer, where AW intersects the continental slope, and at the lee side of a topographic irregularity. This indicates that mixing with ambient colder water along the continental margins is an important contribution to AW heat loss. Furthermore, the cold halocline layer receives approximately the same amount of heat due to upward mixing from the AW, compared to heat input from the summer-warmed surface layer above. This underlines the importance of both surface warming and increased vertical mixing in a future ice-free Arctic Ocean in summer.

Plain Language Summary Warm water from the Atlantic Ocean enters the Arctic Ocean through the Barents Sea and the Fram Strait, between Greenland and Norway, and directly influences the formation of sea ice: When the Atlantic Water (AW) is located close to the ocean's surface, as is the case shortly after its inflow in the Barents Sea, sea ice melts and new sea ice formation is hindered. This is why the Barents Sea is often ice free, even in winter. Further along the pathway, in the Laptev and East Siberian Sea study region, the AW gradually cools and dives down to deeper layers. In order to quantify the cooling and to understand how and where it happens, we measured vertical profiles of temperature and heat fluxes along a 2,500 km long part of the AW pathway. Based on these measurements, we found that the heat loss mainly occurs by mixing of warm AW with ambient cold water above the continental slope, in particular in the highly energetic region near the sea floor.

1. Introduction

Warm water from the Atlantic provides the main source of oceanic heat for the Arctic Ocean and could melt the entire ice cover if released to the surface (Aagaard et al., 1987; Nansen, 1902; Rippeth et al., 2015; Rudels et al., 2012; Turner, 2010). The Atlantic Water (AW) enters the Arctic through the Fram Strait and the Barents Sea, and propagates with the Arctic Boundary Current (ABC) cyclonically along the Arctic continental margins (Rudels et al., 2012; Schauer et al., 1997). In the Barents Sea and north of Svalbard, the AW is warmer than the near-freezing polar waters and occupies the near-surface layer of the water column, delaying sea ice formation and melting ice that is advected into the region (Meyer et al., 2017; Smedsrud et al., 2013). This sea ice melt leads to a gradual cooling and freshening of surface waters, and subsequently to subduction of the eastward propagating AW. The Barents Sea branch of the AW exits the shelf regions mainly through St. Anna Trough and joins the eastward propagating Fram Strait branch. A

strongly stratified cold halocline layer now insulates the surface ocean and sea ice from the subducted AW, and inhibits turbulent mixing and vertical heat loss to the upper layer. A recent analysis of observations (2013–2015) discussed the progression of conditions typically found north of Svalbard, where warm and saline water of Atlantic origin is in direct contact with the surface layer, far into the eastern Eurasian Basin, up to 1,500 km along the AW pathway (Polyakov et al., 2017). In the light of the changing Arctic Ocean, it is increasingly important to investigate and understand the fate of the heat carried in the AW, and quantify the vertical (and lateral) mixing rates.

Direct shear-based turbulence measurements needed to quantify vertical mixing and heat fluxes are still comparatively scarce in the Arctic Ocean, but are urgently needed to improve our understanding of mechanisms driving changes in the ocean and sea ice system and to constrain parameterizations used in numerical models. The upper AW layer in the eastern Arctic Ocean interior basin is characterized by low turbulent dissipation rates and the presence of thermohaline staircases, and vertical fluxes are hence largely dominated by diffusive convection (Lenn et al., 2009; Polyakov et al., 2019; Rainville & Winsor, 2008; Shibley et al., 2017). Reported average vertical heat flux estimates in the central Amundsen Basin range from 0.2 W m^{-2} (Fer, 2009, turbulent heat flux above the thermocline, April 2007), 0.33 W m^{-2} (Guthrie et al., 2017, diffusive convection, April 2013), 0.3 W m^{-2} (Guthrie et al., 2017, turbulent heat flux, April 2014) to 0.6 W m^{-2} (Sirevaag & Fer, 2012, diffusive convection, April and August 2008). In contrast to the calm interior region, the interaction of tidal currents and the topography at the upper continental slope bears the potential for high vertical mixing rates. Tidal currents exhibit much higher amplitudes at the basin margins, compared to interior regions (Baumann et al., 2020), and Rippeth et al. (2015) found turbulent dissipation rates to be enhanced by up to two orders of magnitude above the steep continental slope. Lenn et al. (2011) identified tidally driven intermittent high turbulent dissipation rates in the near-bottom layer and in the pycnocline above the Laptev Sea continental slope. Renner et al. (2018) suggest that tidal mixing on the upper slope is an important factor for the cooling of the AW Boundary current north of Svalbard. A mechanism for the conversion of tidal energy to turbulent mixing on the Arctic continental slope is the generation of trapped lee waves by the displacement of isopycnals during cross-slope tidal flows, and the subsequent energy release as described in Fer et al. (2020). The isopycnal displacement associated with this process generates a surface signal that can be identified in satellite images, showing the frequent occurrence along the Arctic shelves. Fer et al. (2020) hypothesize that the contribution of spatially confined tidally driven slope mixing to the heat loss from the AW layer is comparable to the Arctic-wide heat loss by double diffusion. North of Svalbard, where the AW still resides close to the ocean surface, reported values of the mean heat flux over the AW thermocline are 17 W m^{-2} (Meyer et al., 2017, N-ICE2015 campaign January to June 2015), with much higher values of more than 100 W m^{-2} during storm events. This is in line with an estimated average heat loss of the boundary current of 16 W m^{-2} in this region (Renner et al., 2018). Further along the ABC pathway, above the East Siberian continental slope, double diffusive heat flux estimates of ~1 W m^{-2} from 2007 were an order of magnitude lower than the heat fluxes required to account for the observed cooling of the ABC (Lenn et al., 2009). Mixing with cold shelf water at the upper continental slope was identified as an important cooling process of the AW along the continental margins, but not resolved in the observations (Lenn et al., 2009). Still, the characteristics and mechanisms of boundary mixing in this region are poorly understood.

In this study, we present a comprehensive collection of temperature profiles and direct vertical heat flux measurements, obtained on 11 cross-slope transects across the ABC pathway between St. Anna Trough and the East Siberian Sea in summer 2018. We aim to quantify the along-slope heat loss of AW and to understand the relative importance of the dominant cooling processes in the summer season. The paper is organized as follows: Section 2 presents the data and methods applied in Section 3, where we highlight the variability of AW in the study area and quantify the heat loss along its pathway, before presenting direct estimates of vertical heat fluxes. In Section 4, we discuss our results in the context of previous studies, and conclude the paper in Section 5.

2. Data and Methods

2.1. Observations

Data presented in this study were obtained during an expedition aboard the *Akademik Tryoshnikov*, August 18 to September 29, 2018 to the Eurasian Basin and continental slope region of the Laptev and East Siberian
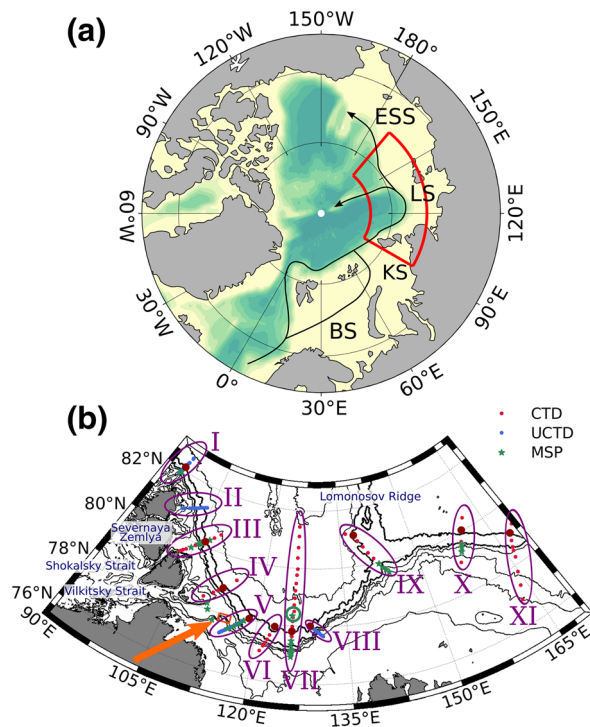
Figure 1. (a) Bathymetric map of the Arctic Ocean, with the schematic pathway of the Atlantic Water (AW) indicated in black, and the study area indicated in red. The Barents Sea (BS), Kara Sea (KS), Laptev Sea (LS), and East Siberian Sea (ESS) are marked for better orientation. (b) Enlargement of the study area with conductivity, temperature, and depth (CTD, red dots), underway CTD (UCTD, blue dots) and microstructure (green stars) stations indicated. Individual transects are identified with roman numerals. The green circle marks the position of the 24 h microstructure station. The 50, 100, 200, 500, 3,000, 4,000, and 5,000 m isobaths are indicated in thin lines, 1,000 and 2,000 m in thick lines. Big dark red dots indicate the CTD stations used for Figure 6 (Section 3.1), the orange box and arrow mark the approximate location of the 10 h station (Section 3.2). Bathymetric data was taken from the International Bathymetric Chart of the Arctic Ocean (IBCAO) data set (Jakobsson et al., 2012).

Seas. The expedition included jointly organized research activities between the US-Russian NABOS (Nansen and Amundsen Basin Observational System) program and the German-Russian CATS (Changing Arctic Transpolar System) projects as part of the "System Laptev Sea" partnership. The Laptev and East Siberian Sea were mostly ice free during the measurement period; only some stations in the north-eastern part of the study region were carried out in the marginal ice zone (see Tarasenko et al., 2019, for details).

High-resolution temperature, salinity and shear velocity measurements were performed from the ship (green stars labeled "MSP" in Figure 1), with a tethered microstructure profiler (MSS 90L, Sea & Sun Technology, Germany) that was free-falling with a sinking velocity of approximately 0.6 m s^{-1}. The length of the tether restricted profiles to approximately 350 m water depth. The microstructure profiler sampled at 512 Hz and was equipped with precision conductivity, temperature, depth (CTD) sensors (Sea & Sun), a fast-responding temperature sensor (FP07), two airfoil shear probes (PNS06 from ISW, Germany), and additional fluorescence and turbidity sensors. The sensors were protected with a steel cage that allows for profiling very close (less than 0.1 m) to the sea bed. The cage can generate flow disturbances of high frequency, which are well separated from the turbulence signals in the frequency domain, and do not impact the estimation of turbulent dissipation rates. The typical noise level of the MSS shear probes is 5×10^{-10} to 1×10^{-9} W kg^{-1}. For robust estimates of turbulence, one microstructure station comprised at least three individual casts. In addition, a 10 h microstructure time series was collected over the continental slope east of Vilkitsky Strait (orange box in Figure 1b), as well as a 24 h-time series station further offshore on the 126°E transect (see Figure 1b), which was performed between 18 and 20 September 2018, and interrupted by a 9 h instrument repair break.

In addition to the microstructure casts, a total of 145 vertical CTD profiles were measured with a Seabird 911 CTD rosette sampler, at a sampling rate of 24 Hz (red dots in Figure 1b). All data were averaged to 1 dbar resolution using the Seabird processing software. No correction for salinity with water samples in the laboratory was performed on board. The initial sensor accuracy given by the manufacturer is ± 0.001°C for the temperature, and ±0.0003 S m^{-1} for conductivity. The difference of the duplicate temperature and conductivity sensors in low-gradient deep waters were well below the given accuracy: 5×10^{-4}°C and 2.2×10^{-4} S m^{-1}, respectively, and 3.5×10^{-3} for salinity. During six ship transits between sampling regions, additional transects with a horizontal spacing of 1–10 km were obtained with an underway CTD (UCTD, manufactured by Ocean Science), sampling at 16 Hz (blue dots in Figure 1b). The accuracy given by the manufacturer is ± 0.004°C for temperature and ±0.05 for salinity. The calculation of derived quantities was implemented using the TEOS-10 set of sea water equations (McDougall & Barker, 2011). Throughout this paper, temperature (θ) refers to conservative temperature and salinity to absolute salinity.

Current velocity data are available from a cross-slope mooring array of upward looking 75 kHz (4 m vertical resolution) and 150 kHz (8 m) Acoustic Doppler Current Profilers (ADCPs, Teledyne RDI), deployed at 95°E (transect I), between August 2015 and 2018; and from upward looking 75 kHz ADCPs (Teledyne RDI) along the 126°E transect, deployed between September 2015 and 2018. Exact positions and additional information can be found in Table 1. The depth-averaged current from all ADCP measurements was directed approximately to the east (within a range of 30°), and the major direction of the current is assumed to represent the along-slope boundary current speed. The tidal variability was bounded within the M2 frequency band (1.9–2 cycles per day) and was removed from the time series using a 100-h running average.

Table 1
Positions and Water Depth, Profiling Range, Vertical and Temporal Resolution and Deployment Period of the Moored Acoustic Doppler Current Profilers North of Severnaya Zemlya (AK–Moorings) and at the 126°E Transect (M–Moorings)

ID	Position	Depth	Range	Resolution	Start	Recovered
AK1	81.84°N, 94.32°E	300 m	22–222 m	4 m/90 min.	August 25, 2015	August 28, 2018
AK2	81.90°N, 94.48°E	900 m	28–280 m	4 m/90 min.	August 25, 2015	August 25, 2018
			279–831 m	8 m/90 min.		
AK3	81.96°N, 94.54°E	1,400 m	24–232 m	4 m/90 min.	August 25, 2015	August 25, 2018
			233–753 m	8 m/90 min.		
AK4	82.10°N, 94.77°E	1,900 m	49–465 m	8 m/90 min.	August 25, 2015	August 24, 2015
AK5	82.22°N, 94.85°E	2,300 m	9–83 m	4 m/90 min.	August 25, 2015	August 23, 2018
			91–307 m	8 m/90 min.		
M1$_1$	77.07°N, 125.82°E	252 m	20–230 m	5 m/60 min.	September 18, 2015	September 4, 2018
M1$_2$	77.17°N, 125.79°E	783 m	201–456 m	5 m/60 min.	September 18, 2015	September 4, 2018
M1$_4$	78.46°N, 125.96°E	2,700 m	163–428 m	5 m/60 min.	September 20, 2015	September 19, 2018

2.2. Definition of Water Layers

In the following analysis, the water column is divided into different layers, based on the measured temperature and salinity profiles (as an example, see Figure 2 in Section 3.1 and Figure 9a in Section 3.2). Following Polyakov et al. (2017), the base of the surface mixed layer (SML) is identified by a change of water density from the surface value of 0.125 kg m^{-3}. Below the SML, the cold halocline layer is defined using the density ratio:

$$R = \frac{\alpha\Delta\theta}{\beta\Delta S} \tag{1}$$

where α is the thermal expansion and β is the haline contraction coefficient. The cold halocline base is then defined as the threshold of $R = 0.05$ (following Bourgain & Gascard, 2011). The lower halocline layer below extents to the depth where strong temperature gradients characterize the transition to AW. This "AW thermocline" layer (in contrast to the thermocline below the SML) is bound by the first depth below the cold halocline layer where the temperature exceeds 0.8 times the minimum temperature in the cold halocline layer, and the first depth where the temperature exceeds 0.8 times the maximum temperature of the AW layer (see Figure 9a in Section 3.2). This AW thermocline is not the same as the AW layer, which is often defined as the layer between the 0°C isotherms (Polyakov et al., 2017), or based on density (1027.70–1027.97 kg m^{-3}) and potential temperature (>2°C) (Rudels et al., 2000). Thermohaline staircases, which are found at the depth of the AW thermocline at some stations, were visually identified.

The upper ocean heat content (in J m^{-2}, displayed in Figure 7) is calculated according to

$$\text{heat content} = \rho_0 c_p \int_{z=30m}^{300m} (\theta - \theta_f)dz, \tag{2}$$

where θ_f is the (salinity and pressure dependent) freezing temperature, $\rho_0 = 1027$ kg m^{-3} is the seawater density and $c_p \approx 3{,}991.9$ J kg^{-1} K^{-1} the specific heat capacity of seawater (Polyakov et al., 2017). The vertical integration range in Equation 2 (also marked in Figure 6a in Section 3.1) is chosen to exclude SML values, which are unrelated to the AW heat dynamics, and to cover the layer where most of the temperature loss takes place along the ABC pathway.

The distance between two neighboring transects Δx is calculated along the 2,000 m isobath (thick black line and big red dots in Figure 1b), using the International Bathymetric Chart of the Arctic Ocean (IBCAO) topography without smoothing. Using this distance and the difference in upper ocean heat content, the heat loss between adjacent transects can be calculated. To account for the bifurcation of the current at the
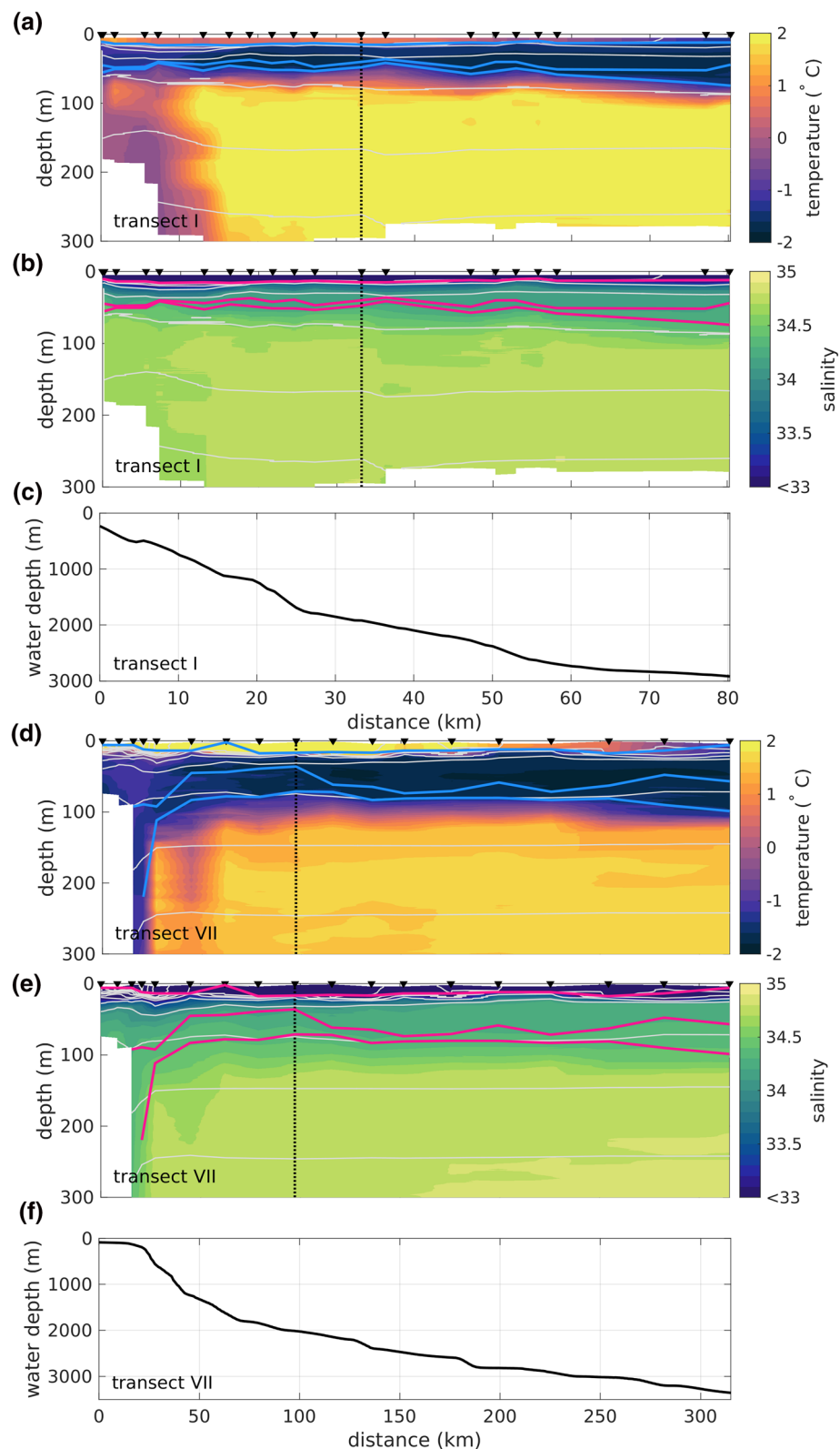
Figure 2. Exemplary (a and d) temperature (°C), and (b and e) salinity measurements along the (a and b) 95° E transect I and (d and e) the 126° E transect VII (2D linearly interpolated). IBCAO depth along each transect is displayed in (c) and (f), respectively. White lines indicate isopycnals with a spacing of 0.5 kg m^{-3}, blue/red lines indicate the depth of the surface mixed layer, the base of the cold halocline layer, and the beginning of the AW thermocline as defined in section 2.2. The vertical dashed line indicates the position of the 2000 m isobath.
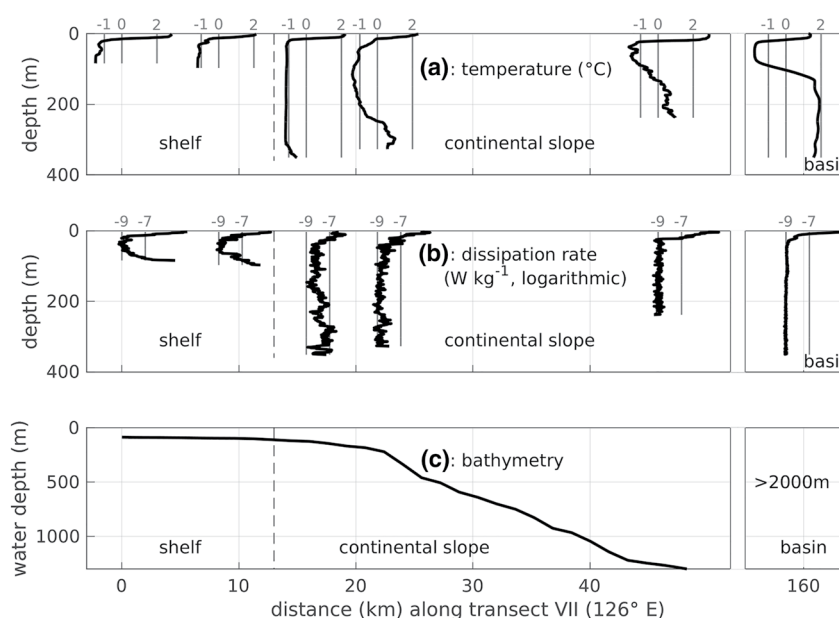
Figure 3. Exemplary vertical profiles of (a) temperature (°C) and (b) turbulent dissipation rate (W kg^{-1}) along the 126°E transect (transect VII). In (c), the bathymetric slope is displayed.

Lomonosov Ridge, the heat loss on the first East Siberian Sea transect X is calculated relative to the last transect with sufficient data cover before the ridge (VII).

2.3. Microstructure Data Processing and Heat Flux Calculation

In the postprocessing of the microstructure profiler data, signals from the respective sensors are corrected for their relative vertical displacement (i.e., different mounting height on the probe), with the shear sensors as reference level. The lower end of each profile is identified either by the largest negative acceleration (when the profiler reaches the sea floor) or when the sinking speed falls below 0.3 m s^{-1} (deceleration by tension on the cable when the profile is terminated before reaching the sea floor). In each raw data channel, data points that exceed 3 times the standard deviation, calculated over 40 data points, were identified as outliers, removed and linearly interpolated.

The dissipation rate ε is calculated independently from each shear sensor by fitting Nasmyth's universal turbulence spectrum (Nasmyth, 1970) to the power spectrum of subdivided sections of 512 data points, after removing the linear trend from each subsection. The results derived from the two shear sensors were subsequently averaged, where again data points were discarded when the individual dissipation estimates differed by a factor of 5. All data were subsequently averaged to 1 m vertical resolution.

Unfortunately, no direct current velocity measurements are available contemporaneous with the micro-structure profiles. Following Becherer et al. (2015), the bottom friction velocity u_* can be calculated from the dissipation measurements for the profiles covering the whole water column down to the seabed (stations on the shelf and all except for the first four profiles of the 10 h station, Section 3.2), using the law-of-the-wall relation

$$u_* = \left[\kappa \varepsilon z \right]^{\frac{1}{3}}, \tag{3}$$

where $\kappa = 0.41$ denotes the von Kármán constant and z the height above bottom. As this relation is only valid in the well-mixed near-bottom layer, only the lowermost two bins, corresponding to the lowermost 2 m of the water column, were used for the calculation.

The calculation of vertical heat fluxes from the microstructure data requires the turbulent diffusivity
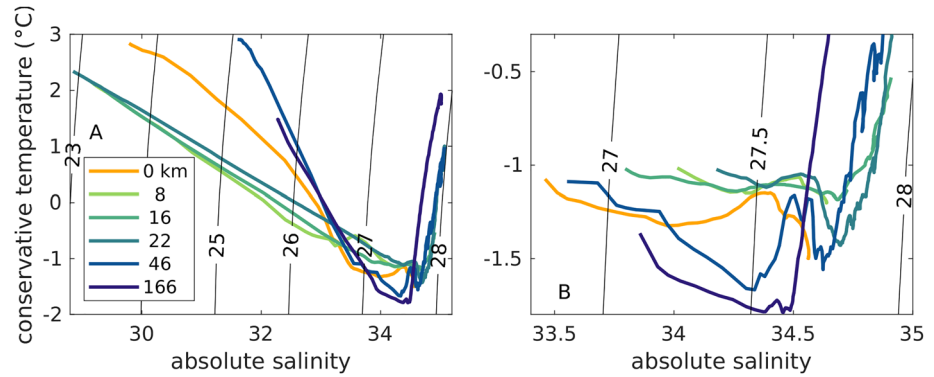
Figure 4. (a) T-S diagram of the selected stations along transect VII (126° E, corresponding to the profiles displayed in Figure 3), (b) T-S diagram of the same stations, but excluding SML values. Colors indicate the respective distance along the transect of the profiles in km.

$$K_\rho = \Gamma \frac{\varepsilon}{N^2}, \tag{4}$$

where ε denotes the dissipation rate and N the buoyancy frequency. The canonical value of the mixing efficiency, $\Gamma = 0.2$, was introduced as an upper limit by Osborn (1980), and its general validity has since then come under debate. In a recent review, Gregg et al. (2018) suggest that applying the canonical constant value for the mixing efficiency still leads to a better agreement between K_ρ derived from microstructure and tracer release experiments, compared to parameterizations derived in simulations or in the laboratory. Even though the reasons for this agreement are not understood, Gregg et al. (2018) suggest that observations should generally continue to be scaled with $\Gamma = 0.2$. In two regimes considered in this study, however, the choice of Γ requires further attention:

1. The model of Osborn (1980) explicitly excludes double diffusive phenomena, which are certainly of importance at the upper bound of the AW layer. Several studies suggest that the mixing efficiency in regions exhibiting double diffusive convection (or salt-fingering), where turbulence is driven by buoyancy fluxes rather than shear, is higher than the canonical value (Inoue et al., 2007; Lee et al., 2014; Nakano & Yoshida, 2019; Padman, 1994; St. Laurent & Schmitt, 1999, and the references therein). Based on data from the Laptev Sea in 2007 and 2008, Polyakov et al. (2019) report an optimal value of $\Gamma = 1$ to quantify heat fluxes at the upper bound of the AW layer, in the presence of both well-defined and degraded thermohaline staircases. Hence, $\Gamma = 1$ will be applied for the calculation of K_ρ *only* in the AW thermocline. For a direct comparison with heat flux estimates that were based on the canonical value of Γ, e.g., Meyer et al. (2017), values reported in this study must consequently be divided by a factor of 5.

2. A widely used parameterization of Γ introduced by Shih et al. (2005) suggests reduced mixing efficiencies in highly turbulent and weakly stratified regions, such as the near-bottom domain considered in this study. This validity of this parameterization is, however, under debate (Gregg et al., 2018, and the references therein). While another study reports mixing efficiencies higher than the canonical value in the bottom mixed layer over sloping topography (Slinn & Riley, 1996), Scotti and White (2016) suggest that $\Gamma = 0.2$ is valid also in turbulent boundary layers. In the absence of a conclusive agreement, K_ρ in the turbulent near-bottom layer will be scaled with the canonical value of $\Gamma = 0.2$ in this study.

Using the mixing efficiencies discussed above ($\Gamma = 1$ in the AW thermocline, $\Gamma = 0.2$ otherwise), the turbulent heat flux is then calculated as

$$F_h = \rho_0 c_p K_\rho \frac{d\theta}{dz}, \tag{5}$$

where θ denotes the conservative temperature, ρ_0 and c_p are again the sea water density and the specific heat capacity of sea water, respectively, and the z coordinate is oriented downward from the sea surface (meaning that positive values of F_h correspond to upward heat fluxes). In order to obtain reliable estimates, unaffected
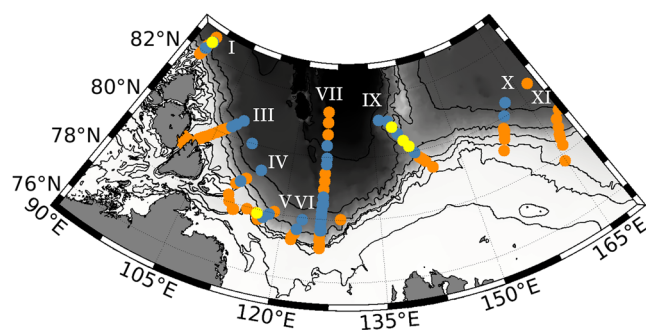
Figure 5. Spatial distribution of CTD profiles with well-defined thermohaline staircases (blue), remnants of thermohaline staircases (yellow) and no thermohaline staircases (orange).

by small-scale temperature inversions, and to get robust estimates for the turbulent dissipation, heat fluxes are calculated as bulk values over the respective layers introduced in Section 2.2, or over the bottom boundary layer. This means that temperature gradients as well as the buoyancy frequency are calculated from the top-to-bottom difference in temperature and density, respectively, and ε is the average value over the whole layer.

3. Results

3.1. A Quasi-synoptic Hydrographic View of the Eurasian Continental Slope in 2018

Vertical profiles of temperature, salinity (Figure 2) and the turbulent dissipation rate (Figure 3b) from the shallow shelf into the deep basin provide insights into the hydrographic structure above the continental slope in summer 2018, and highlight distinct characteristics that allows a categorization of the transects into three distinct subregions:

1. The shallow continental shelf region, where a warm SML (see Section 2.2 for the definition of water layers) overlies an otherwise cold water body. Turbulent dissipation rates are enhanced in both the SML and bottom boundary layer, and close to the noise level in the interior water column.

2. The continental slope region, where (presumably intermittent) patches of enhanced dissipation rates are found throughout the water column, in addition to the turbulent boundary layers. The temperature gradient at the upper boundary of the AW layer is less sharp than in the interior basin, and the 0° isotherm is located increasingly deeper in the water column toward the shallower parts of the slope. At some of the upper slope stations, temperatures throughout the halocline are higher compared to stations on the shelf or in the basin, indicating strong vertical mixing (Figure 4). In the presence of very high dissipation rates (up to 10^{-7} W kg^{-1}, third profile in Figure 3), temperature profiles can be nearly homogeneous in the vertical. In general, both the vertical and cross-slope temperature distribution above the continental slope are heterogeneous and exhibit small-scale disturbances such as intrusions, overturns and isolated warm water cores (Figure 2).

3. The interior basin, where the upper water column exhibits the classical structure of a (warm) SML overlying the cold halocline layer, and the warm AW layer below, with little lateral variation along the transect except for a vertical displacement of the isopycnals (less than 40 m). Enhanced dissipation rates are generally confined to the SML.

In addition to the general distinction between shelf, continental slope and interior basin regions along each transect, larger-scale spatial gradients are present: The warm and relatively fresh SML exhibits highest temperatures and lowest salinities on the inner shelf, and lower temperatures further offshore (see Tarasenko et al. [2019] for details). The thickness of the SML ranges from 2 to 28 m (on average 12 m), with no distinct spatial trend. In the interior basin, the underlying cold halocline layer is thinner in the western part of the Laptev Sea, compared to the eastern part: West of 135°E (transects I to VIII, Figure 1b), the cold halocline base is mostly located between 30 and 60 m water depth (on average 55 m). East of 135°E, the minimum depth of the CHL base successively increases from 63 m on the "ridge transect" IX (138°E) to 74 m on transect X (160°E) and 81 m on XI (168°E). The average depth of the halocline base east of 135°E is 87 m. The stratification within the cold halocline, however, exhibits no distinct zonal gradients and ranges mostly between $N^2 = 3 - 10 \times 10^{-4}$ s^{-2} (on average 6.2×10^{-4} s^{-2}). Away from the continental slope, the 0°C isotherm deepens almost linearly with distance from west (60–90 m on transect I) to east (175–220 m on transect XI). Similarly, the maximum AW temperature decreases from 2.5°C on transect I to 1.3°C on transect XI (see Figure 6).

Thermohaline staircases, formed in weakly turbulent conditions by double diffusion at the upper bound of the AW layer, are typically present in the Laptev and East Siberian Seas. Isolated thick (10–50 m) layers of constant temperature and salinity could only be identified in around 30% of the CTD stations (see Figure 5) that were deep enough to cover the typical depth range of the staircases (100–350 m, depending on depth of the AW core, see Figure 6a). These profiles were all located further offshore, and most of the observed stair-
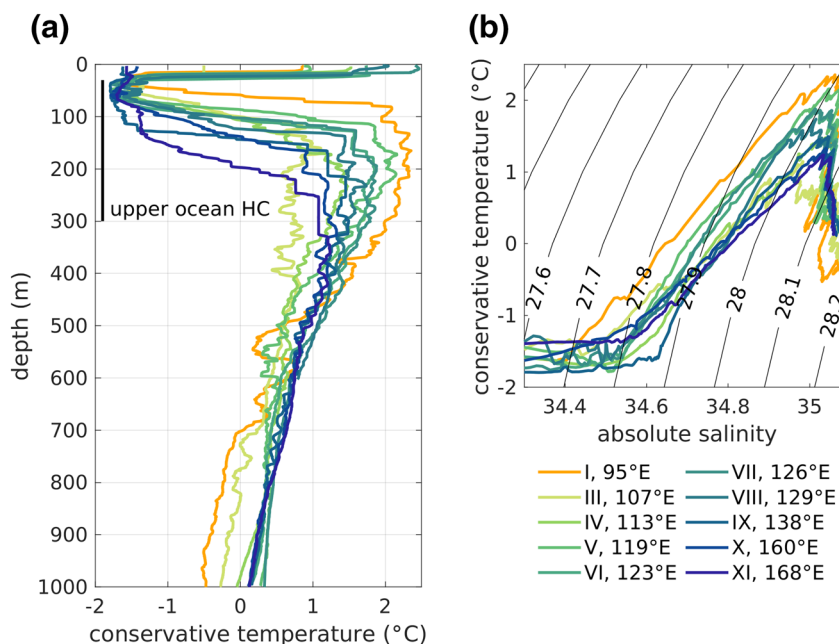
Figure 6. (a) Along-slope temperature profiles at stations closest to the 2,000 m-isobath (stations are indicated in dark red dots in Figure 1) and (b) corresponding T-S diagrams.

cases were not well-defined (i.e., no sharp gradients between the individual layers were present). The microstructure profiles were mostly obtained in the more energetic continental slope region and well-defined staircases with small (less than 7 m) individual layers were only captured at the 24 h station (offshore on transect VII, 126°E) and at the microstructure deepest station on transect IX (138°E, 1,300 m water depth).

To quantify the apparent heat loss from west to east along the ABC pathway, we averaged the upper (30–300 m) ocean heat content for each transect (Figure 7). To avoid biases induced by the heterogeneity of the AW above the continental slope, only temperature profiles from stations at water depths deeper than 2,000 m (away from the continental slope) are considered. Consequently, there are no heat content estimates for transects II, V, and VIII.

The average upper ocean heat loss along the ABC pathway (i.e., the slope of the linear regression displayed in Figure 7) is $\mathcal{O}(10^8)$ J m^{-2} per 100 km travel distance. The relatively high heat loss between transects I and III and transect IV and VI might be explained by dynamics associated with the Shokalsky and Vilkitsky Straits that are located between these transects, respectively (see Figure 1). These straits provide a connection to the Kara Sea and a transport pathway for cold shelf water, on average 0.5–0.7 Sv in summer (Panteleev et al., 2007); and the more complicated topography in the vicinity of these straits potentially increases local mixing (Janout et al., 2015, 2017). A comparatively high heat loss is observed between transects IX and X, where the Lomonosov Ridge forms a potential source of enhanced mixing, and X and XI in the East Siberian Sea. In this region, the continental slope is wider and less steep, which might enhance the area where the AW is in contact with the continental slope and subject to mixing in the turbulent BBL (see Section 3.2), or by a slower progression (and therefore a longer travel duration) of the ABC in the East Siberian Sea. The small heat gain between transects III and IV might be attributed to an intermittent offshore advection of the AW layer in the vicinity of Shokalsky Strait, as indicated by a less pronounced AW core with lower maximum AW temperature on transect III (light green line in Figure 6a) compared to the profiles from adjacent transects.

An average current velocity at the depth of the AW layer can be estimated from the data of the moored ADCPs, displayed in Figure 8. Across transect I at 95°E, the main current direction from all ADCP records is generally eastwards, more or less aligned with the isobaths in this region. Current speeds (averaged over the whole three year deployment period) at the three deep moorings range from 0.06 to 0.1 m s^{-1} (gray patch in Figure 8a),
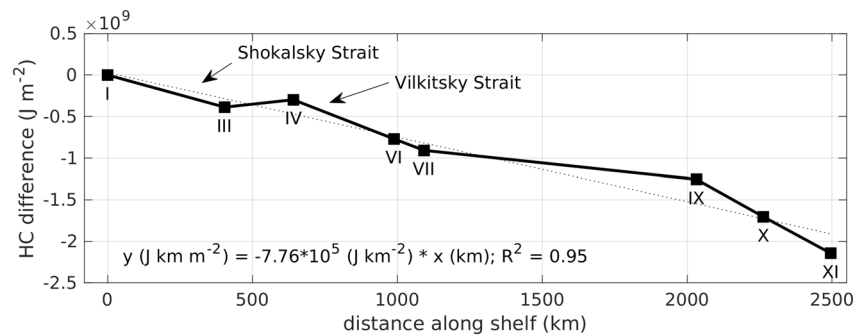
Figure 7. Difference in upper ocean (30–300 m) heat content (HC), relative to transect I, averaged over all CTD profiles obtained at water depths greater than 2,000 m on each transect. The dotted line shows the linear regression, equation and coefficient of determination R^2 of the linear regression are noted.

and are approximately homogeneous in the vertical. Only a small trend toward higher current velocities at shallower positions is visible at the three deep positions, but current velocities at the upper slope (above 900 m, moorings AK1 and AK2) are considerably higher, up to 0.4 m s^{-1}. This trend toward higher velocity magnitudes at the upper slope, up to 0.15 m s^{-1}, can also be observed at the 126°E transect VII.

Based on the ADCP data, we assume an average boundary current propagation velocity of 0.08 m s^{-1}, derived from ADCP data of moorings AK3–AK5, at transect I (95°E) in the 3 years prior to the ship-based observations in 2018 (for further discussion, see Section 4.1). Pnyushkov et al. (2015) found that the magnitude of the propagation speed decreases along the ABC pathway, and is twice as high in the western compared to the eastern Laptev Sea. Assuming a linear decrease of the propagation speed within the Laptev Sea results in a correction factor of 0.75 to obtain an average Laptev Sea propagation speed (0.06 m s^{-1}) from velocity estimates at transect I. Based on this average, the heat flux needed to account for the observed mean heat loss is approximately 47 W m^{-2}. This calculated heat flux, however, depends linearly on the assumed boundary current velocity, which forms a considerable source of uncertainty (see Section 4.1).

3.2. Vertical Mixing and Heat Fluxes

3.2.1. Interior Basin

Over 90 profiles were measured during the 24 h microstructure station, located offshore (deeper than 2,000 m) on the 126°E transect (see Figure 1b). Temperature profiles over the measurement period exhibited only little variability, except for a vertical isopycnal displacement of ∼20 m throughout the water column. Thick thermohaline staircases up to 40 m are visible below the AW thermocline (Figure 9a). Within the thermocline layer, several staircase layers of a few meter thickness are present. During the measurement period, these small staircases were not always well-defined, but intermittently degraded. Turbulent dissipation values are slightly elevated around the AW thermocline (Figure 9b). The strong temperature gradients combined with enhanced dissipation rates, induce an enhanced heat flux of on average 10 W m^{-2} over this layer. The small negative (i.e., downward) heat flux observed in the CHL indicates that the halocline region receives some heat from the warm SML above. The upward heat flux in the lower halocline is approximately three times larger than the heat input from the SML. At the only other station deeper than 2,000 m (on transect III, see Table 2), a smaller heat flux of 3.2 W m^{-2} over the AW thermocline was found.

3.2.2. Continental Slope

Similar to the analysis of the 24 h station, we obtain heat flux estimates for the continental slope region for the different layers of the water column by averaging all heat flux estimates from microstructure profiles along the transects (Table 2). An average upward heat flux of 3.7 W m^{-2} is observed in the AW thermocline, smaller than the corresponding heat flux observed further offshore (at water depths greater than 2,000 m). The negative heat flux in the cold halocline layer indicates a warming of this layer caused by the presence of a warm SML water above, nearly equal to the upward heat flux in the lower halocline layer below. The

Table 2
Vertical Heat Fluxes (W m^{-2}) for the Microstructure Stations on the Transects (Excluding Shelf Stations, Where the Water Layer Definition Cannot be Applied, and excluding the 10 hour and 24 hour station). Averages refer to the averages over all stations at positions shallower than 2000 m.

	Cold halocline layer	Lower halocline	AW thermocline	Water depth (m)
Average	**−0.4 ± 0.6**	**0.3 ± 0.6**	**3.7 ± 1.8**	
Transect I (95°E)	−0.8	2.5	6.4	701
	−0.3	0.3	2.2	1,035
Transect III (107°E)	−0.1	0.0	1.6	362
	−0.1	0.2	4.8	587
	−0.3	1.5	7.1	887
	[a]	−0.1	2.9	1,067
	[a]	−0.1	2.8	1,845
	−0.1	0.2	3.2	2,384
Transect V (119°E)	−0.4	0.1	3.9	287
	−0.3	0.1	5.1	955
	−0.3	0.2	5.1	1,480
Transect VII (126°E)	−0.8	0.1	2.8	207
	−0.6	0.1	6.9	429
	−2.8	0.0	1.6	1,266
	−0.3	0.2	3.9	1,542
Transect IX (138°E)	−0.0	0.1	3.0	1,329
Transect X (160°E)	−0.1	0.2	2.0	302
	−0.1	0.2	2.2	405
	−0.0	0.1	2.6	967

[a]Thickness of cold halocline layer only a few meters, hence no heat fluxes calculated.

individual heat fluxes at each station (Table 2) differ in magnitude, but exhibit the same general pattern of a comparably large upward heat flux in the AW thermocline, a small upward heat flux in the lower halocline and a downward heat flux in the cold halocline layer.

3.2.3. Heat Loss in the Turbulent BBL

On August 28, 2018, 10 h of continuous microstructure measurements were performed at the northwestern Laptev Sea slope, starting at 114°E 26.9′, 77°N 56.8′, while the ship was freely adrift under moderate (8 m s^{-1}) westerly winds. The eastward drift started at a water depth of 340 m, and reached a southernmost position near the 250 m-isobath around 19:00, before moving north again (Figure 10a). The drift track roughly follows the contemporary modeled barotropic tidal currents derived from AOTIM-5 (Figure 10b, [AOTIM-5 Padman & Erofeeva, 2004, updated version from 2018]).

The temperature distribution shows some interesting small-scale variability above the continental slope throughout the drift (Figure 11a). A warm (up to 3.4°C), approximately 20 m-thick SML overlies a 100–150 m thick cold (−1.0°C) halocline layer, that is vertically bound by a thin, colder (−1.5°C) layer. The thin cold layer further offshore (observed during the first 4 h of measurements, Figure 11a) is less dense due to a 0.1 lower salinity, and is located 40–50 m higher up in the water column compared to the coldest layer further onshore. Below this minimum temperature layer, which had likely been formed on the continental shelf during winter, traces of warmer water are present in the deeper parts.

Turbulent dissipation rates (Figure 11b) are higher near the bottom, up to 10^{-4} W kg^{-1}, but the height of the turbulent BBL is not homogeneous and sometimes not well defined in individual profiles. To obtain a length scale needed to calculate the BBL heat fluxes, an average height of the BBL of 15 m is derived from the average of all dissipation profiles: All individual profiles were aligned at the sea bed using the respective absolute water depth of each cast, and the upper bound of the near-bottom layer was identified as the vertical position where ε reaches the background value ($\varepsilon < 10^{-9}$ W kg^{-1}).

Enhanced near-bottom heat fluxes were found at the lee side of a small sill (at least 10 m high, based on the water depth derived from the microstructure casts), between 13:00 and 14:00; and at the onshore end of the drift, between 18:00 and 20:00 (Figure 11c), where both relatively warm water from a deeper layer and cold halocline water were present within the turbulent BBL. At the lee side of the sill, the extraordinarily high heat flux is confined to only the first microstructure cast behind the sill, whereas the turbulent kinetic energy in the BBL, reflected in the friction velocity u* (green line, Figure 11c), is further increasing with distance from the sill (between 14:00 and 15:00). The (thermal) stratification within the BBL, however, vanishes in the presence of these high dissipation rates, leading to a negligible heat flux in this part of the drift station. The heat flux at the station furthest onshore, at 19:00, is very small because no temperature gradients were present near the bottom in this profile. The small heat fluxes at the beginning (before 13:30) and end (after 20:00) of the drift resulted from low values of turbulent dissipation, reflected in low bottom friction velocities u_*.

4. Discussion

4.1. Uncertainties in Quantifying Heat Loss in the ABC

One aim of this study was to relate the measured vertical heat fluxes to the observed heat loss within the ABC, in order to identify mixing hotspots and assess the relevance of vertical mixing for the distribution
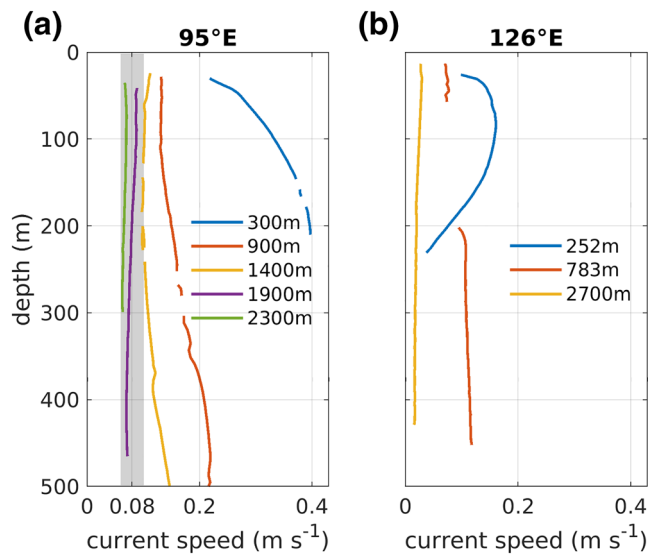
Figure 8. Average (over 3 years, see Table 1) vertical profiles of the current velocity magnitude at different positions along (a) the 95°E and (b) the 126°E transect. The gray patch in (a) marks current velocities between 0.06 and 0.1 m s^{-1}.

of AW heat. Our estimates significantly rely on the calculated average boundary current heat loss of $\mathcal{O}(10^8)$ J m^{-2} per 100 km propagation distance (Section 3.1), and the associated average heat flux of 47 W m^{-2} (based on the exact value of the linear regression in Fig. 7) needed to account for this cooling along the ABC pathway. Hence, the ABC heat loss estimates are crucial but depend on a number of assumptions. The upper ocean heat content depends on the choice of the vertical integration range: The SML (maximum depth of 28 m) must be excluded, as the surface ocean is impacted by atmospheric warming, which is unrelated to the AW heat content. Furthermore, the part of the AW layer that exhibits the largest temperature variability (starting at a depth of 30 m on transect I) needs to be included. The depth range of 30–300 m is an appropriate choice for our study: A smaller vertical range (e.g., 100–250 m, Lenn et al., 2009) does not cover the warm AW core throughout the study area, and an increase of the bottom range (e.g., from 300 to 400 m) results in a spatially uniform increase in HC, and has thus little effect on the calculated heat loss. The sensitivity of the heat loss estimates to the upper bound (30 vs. 50 m or SML depth) is less than 5%.

Additionally, the way of calculating the distance between adjacent transects imposes some uncertainty. Directly following the 2,000 m isobath, as done in this study, the average heat loss amounts to -0.8×10^8 J m^{-2} per 100 km. This might be a slight underestimation, as the general ABC pathway might not be influenced by the finer structures in the topographic slope. By calculating only the direct distance between the station closest to 2,000 m water depth on each transect results in a certainly overestimated heat loss of -1.2×10^8 J m^{-2} per 100 km. The order of magnitude of 10^8 J m^{-2} per 100 km travel distance, however, is reliable.

Further uncertainties arise from the small-scale variability in the temperature profiles. The upper ocean heat content for stations at the upper continental slope region is much smaller compared to undisturbed profiles in deeper waters (see Figures 2a,d and 3a). This smaller heat content is likely a result of enhanced vertical mixing and lateral mixing with ambient shelf water, and hence reflects local mixing processes rather than the progressive cooling of the AW along its pathway. For stations at water depths deeper than 2000 m, the lateral variability in the temperature profiles, and hence the variability of the upper ocean heat content, becomes small on all transects. By considering only stations at a water depth greater than 2000 m for calculating the average heat content per transect, the extremely variable continental slope region is excluded, but in turn, heat content estimates rely on fewer data points per transect. The 126° E transect (see Fig. 2d-f) includes the largest number of deep stations and indicates that the variability in upper ocean heat content is an order of magnitude smaller than the mean value, providing confidence that the discussed heat content estimates are robust, also for transects comprising fewer stations. By including all available profiles per transect into the calculation, the estimated heat loss is reduced by 28 %, and the associated heat flux to account for this reduced heat loss is 34 W m^{-2}.

Assuming a mean propagation speed of 0.06 m s^{-1} (derived from the long-term moorings north of Severnaya Zemlya) over the approximately 2,500 km distance along the ABC propagation pathway between 90 and 165°E, the relative age of the AW varies by slightly less than 1.5 years between the first and the last transect. The properties and volume of the AW inflow into the Arctic Ocean exhibit small temporal trends, and interannual and seasonal variability. The advection of these temperature anomalies within the AW layer can influence the local upper ocean heat content and distort heat loss estimates. A strong positive trend in the AW temperature would appear as heat loss along its propagation pathway, but the small positive trend of +0.06°C year^{-1} for the inflowing AW temperature in the Fram Strait (as reported by Beszczynska-Möller et al., 2012), and +0.04°C year^{-1} in the Barents Sea (Årthun et al., 2012) is much smaller than the temperature decrease of 1.2°C (over approximately 1 to 2 years travel time) observed in the study area. Hence, the effect of a warming trend in inflowing AW is negligible for the heat loss estimate performed in this study.
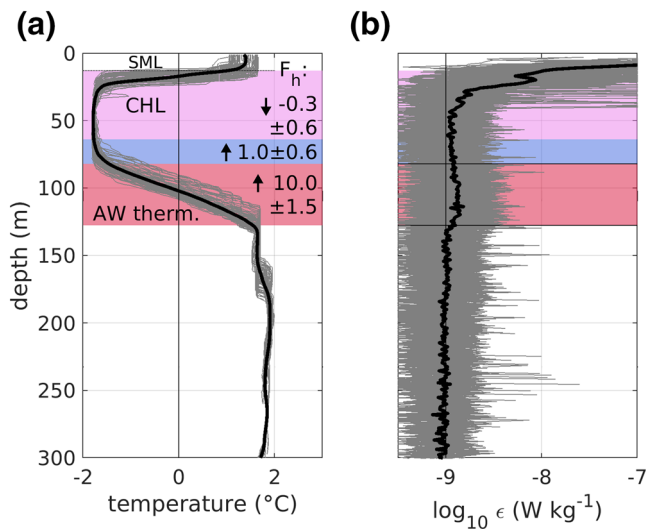
Figure 9. (a) Individual (gray lines) and average (thick black line) temperature profiles obtained during the 24 h station. Indicated are the SML, cold halocline layer (CHL, violet), lower halocline (blue), and the AW thermocline (AW therm., red), and the average and standard deviation of the respective heat fluxes are noted. (b) Individual (gray lines) and average (thick black line) dissipation profiles. $\Gamma = 1$ was applied in the calculation of the heat flux within the AW thermocline.

On annual and seasonal time scales, the variability in AW temperature is larger, approximately 1°C and 2°C, respectively, for AW inflowing through Fram Strait (Beszczynska-Möller et al., 2012); and somewhat larger in the Barents Sea (annual variability approximately 2.0°C, monthly variability around 1.5°C, Boitsov et al., 2012). These temperature anomalies are comparable to the temperature decrease observed in the study area, but due to atmospheric cooling, melting sea ice and mixing, temperature anomalies decrease in magnitude along the AW pathway (the travel time of AW from the Fram Strait to the Laptev Sea is around 6–7.5 years, Beszczynska-Möller et al., 2012). We thus consider the impact on heat loss estimates further downstream to be much smaller. Multiyear hydrographic surveys conducted in the Laptev Sea between 2002 and 2015 show that the core temperature of the AW layer differs by up to 0.9°C during this 13 year time period, and by up to 0.5°C in consecutive years (Zhurbas & Kuzmina, 2020). Zhurbas and Kuzmina (2020) further report a typical cooling of the AW core temperature by 1–2°C per 1,000 km travel distance along the slope, in the area between 31°E and 159°E, which is stronger than the cooling of 1.2°C over approximately 2,500 km travel distance observed in this study. This bias might be due to the further upstream extent of the study area investigated in Zhurbas and Kuzmina (2020), where the cooling is generally stronger (Zhurbas & Kuzmina, 2020). The relatively small temperature anomalies compared to the observed cooling, together with the consistent heat content decrease observed along the AW pathway (Figure 7) give confidence that the estimated heat loss is mainly caused by progressive cooling along the ABC travel pathway rather than upstream variability, in agreement with Lenn et al. (2009).

The results presented in Section 3.1 show that heat is not uniformly lost from the AW along the Laptev and East Siberian slopes. Topographic features such as straits and canyons and potentially the structure of the continental slope itself affect the mixing intensity and thus heat fluxes. The mean heat loss of $\mathcal{O}(10^8)$ J m^{-2} per 100 km along the ABC pathway, obtained with a linear regression accounting for all available heat loss estimates, therefore includes regional over- and underestimations. Nevertheless, considering the robustness of the heat content calculations discussed above, and the high coefficient of determination ($R^2 = 0.95$) of the linear regression (Figure 7), we are confident that this mean heat loss reflects the average cooling of the ABC in the Laptev and East Siberian Seas reasonably well. A comparable study from the eastern Laptev Sea in 2007 reported a heat loss of -0.5 to -1.2×10^8 J m^{-2} per 100 km (Lenn et al., 2009). Repeated surveys north of Severnaya Zemyla (the region between transect I and Vilkitsky Strait in Figure 1) suggested that the AW heat content decreases by 16% over a distance of 350 km (Polyakov et al., 2010; Walsh et al., 2007) in this region. Assuming the same initial HC as estimated from our data on transect I, this decrease would translate to a heat loss of -1.9×10^8 J m^{-2} per 100 km. This number is approximately twice as high as the average heat loss for the Laptev and East Siberian Sea region derived in this study, but consistent with the enhanced heat loss observed in the vicinity of the straits in the Severnaya Zemlya region (Section 3.1). While the ABC propagation speed does not enter upper ocean heat loss calculations, the derived average heat flux of 47 W m^{-2} needed to balance this heat loss (Section 3.1) depends linearly on the assumed mean propagation speed of 0.06 m s^{-1}, inferred from the moored (2015–2018) ADCP data (0.06–0.1 m s^{-1}, Figure 8a), and corrected for its deceleration in the study area. Relatively higher current speeds translate to a shorter propagation time of the AW between the transects, and imply that a higher heat flux is needed to account for the observed cooling. While the estimated current speed is insensitive to the exact vertical depth average (Figure 8), average velocities exhibit a strong variability relative to the measurement position across the bathymetric slope. At the upper slope, below 900 m water depth, average current velocities are around 0.2 m s^{-1} (mooring AK2), and over 0.4 m s^{-1} (AK1) are observed. The amplification of the boundary current velocity at the upper slope is also found at 126°E (Figure 8b, Baumann et al., 2018). As the core of the AW (i.e. the largest mid-water temperature anomalies) is typically found at positions deeper than the 1,000 m isobath (this study, Polyakov
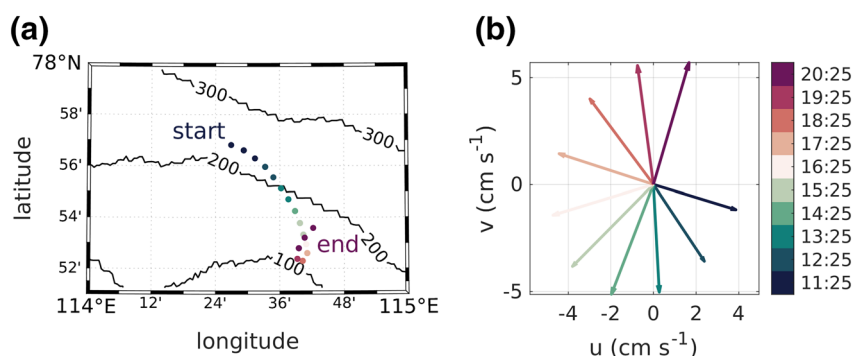
Figure 10. (a) Map indicating the drift track (see the orange box for position in Figure 1) and locations of microstructure profiles (note: the IBCAO bathymetry does not reproduce the actual water depth in this region well, see Figure 11b). (b) Hourly barotropic tidal current from AOTIM-5. Colors indicate the time on August 28, 2018.

et al., 2020a; Zhurbas & Kuzmina, 2020), it is questionable how representative the high current velocities at the upper slope are for the propagation speed of the AW.

A propagation speed of 0.02 m s^{-1} was previously applied in other studies (Dmitrenko et al., 2008; Lenn et al., 2009; Polyakov et al., 2020a), but mean current speeds were reported across a wider range including 0.03 m s^{-1} (from seasonal temperature fluctuations, Coachman & Barnes, 1963), 0.012–0.044 m s^{-1} (from moored current meter data, summer 1995 to 1996, Woodgate et al., 2001), 0.04–0.05 m s^{-1} (moored current profiler, September 2004 to February 2005, Pnyushkov et al., 2013, 2018), and 0.022–0.03 m s^{-1} (Dmitrenko et al., 2008, and the references therein). The comparably high current velocities derived from the moored ADCPs at 95°E are presumably subject to their position at the entrance of AW to the to the continental slope region just downstream of St. Anna Trough, as the ABC propagation speed was shown to decrease along its pathway (Pnyushkov et al., 2015). We account for this effect by applying a correction factor of 0.75, to obtain an average current speed for the whole study are (see Section 3.1). Furthermore, it is likely that the mean ABC propagation speed is subject to spatial heterogeneity and mesoscale dynamics (Pnyushkov et al., 2018; Woodgate et al., 2001), and temporal variability on various time scales, and further efforts to quantify this variability are certainly needed. Considering that the applied mean current speed is based on measurements from the relevant time period and overall agrees with earlier estimates, suggests a reasonable base for our ABC heat loss quantification.

4.2. Mechanisms for AW Cooling

4.2.1. Vertical Heat Flux in the AW Thermocline

The anticipated transition from a quiescent toward a more turbulent state of the Arctic Ocean implies a shift from mainly double diffusive vertical heat transfer to turbulent mixing. A result of this change is the disappearance of thermohaline staircases, which used to be omnipresent in the Arctic interior (Lenn et al., 2009; Polyakov et al., 2020a). Thermohaline staircases were identified in some CTD profiles presented in this study, but they did not exist throughout the (deeper parts of) the study region (Figure 5). While thermohaline staircases are not expected near the energetic shelf break, their absence in the deeper part of the 126°E transect might be a first sign for the above mentioned change in conditions, but more observational data is needed to confirm this hypothesis.

The mean vertical heat flux at the upper AW interface of 10 W m^{-2} in the offshore (based on the 24 h station) and 3.7 W m^{-2} in the onshore regions are larger than previously reported values from the EB. A decade ago, Lenn et al. (2009) found low turbulent kinetic energy dissipation in the eastern part of the study region, and derived diffusion convection heat fluxes (based on Kelley [1990]) of 0.91–1.6 W m^{-2} through thermohaline staircases at the upper AW interface. Based on the same data set and repeated measurements 1 year later, Polyakov et al. (2019) investigated heat fluxes over the high gradient regions within the staircases (i.e., between the vertically homogeneous layers), using both the measured dissipation rate (and $\Gamma = 1$) and the
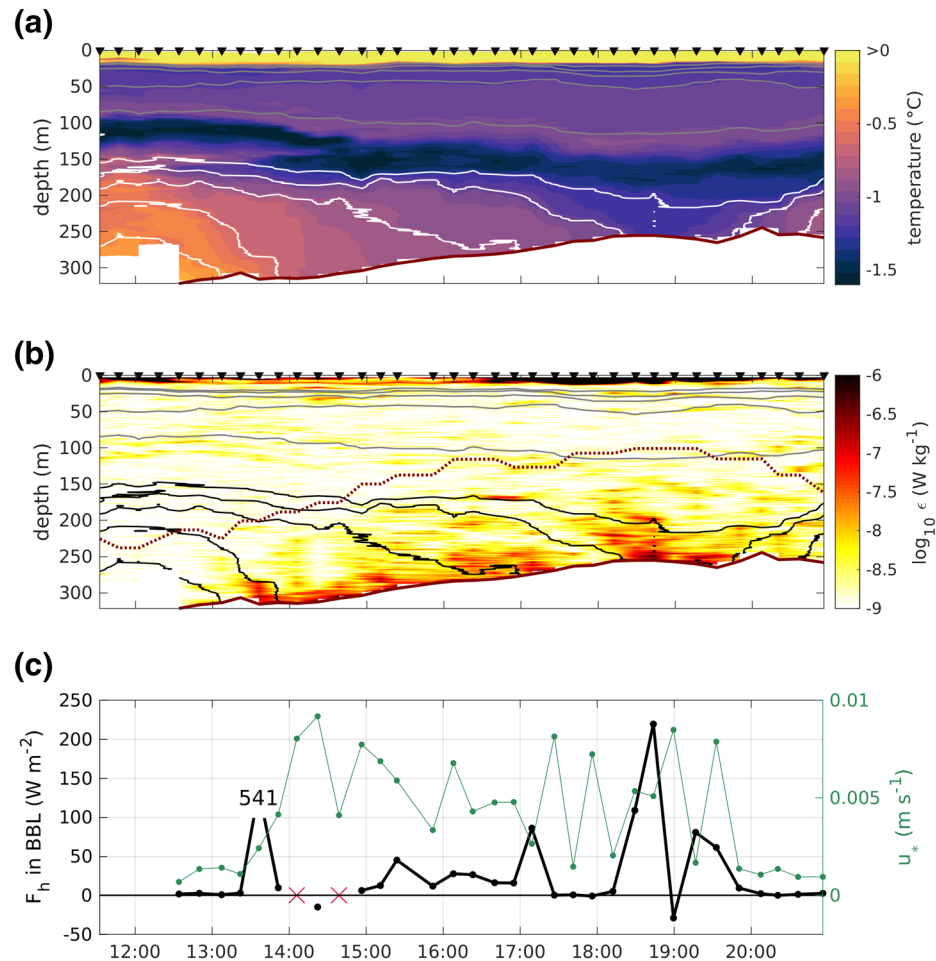
Figure 11. (a) Temperature and isopycnals (equal spacing of gray line: $\Delta\rho = 0.2$ kg m^{-3}, white lines: $\Delta\rho = 0.02$ kg m^{-3}), for the profile locations denoted in Figures 10a and (b) turbulent dissipation rate and isopycnals. The brown lines indicate the real bottom depth, the dotted brown line in (b) the corresponding IBCAO depth. (c) Left vertical axis: Heat flux over the bottom boundary layer (lowermost 15 m), for profiles with unstable stratification the heat flux was set to zero and marked with red crosses. Right vertical axis: bottom friction velocity.

theoretical flux law from Kelley (1990). They inferred heat fluxes on the order of 3–4 W m^{-2} for the high gradient regions of large diffusive layers, but as these large steps are generally overlaid by much smaller steps, characterized by smaller heat fluxes, the overall vertical heat flux from the AW layer was found to be on the order of 0.1–1 W m^{-2}.

Previously reported results of turbulent heat fluxes from the central Amundsen Basin range from 0.2–0.3 W m^{-2} (Fer, 2009; Guthrie et al., 2017; Sirevaag & Fer, 2012). The much larger heat fluxes in the basin of 10 W m^{-2} reported here can partly be attributed to our choice of the mixing efficiency $\Gamma = 1$, which amplifies heat fluxes by a factor of 5 compared to using the canonical value of $\Gamma = 0.2$ applied in most previous studies. Still, an average heat flux of 2 W m^{-2} over the AW thermocline during the 24 h station, using $\Gamma = 0.2$, is an order of magnitude larger than previously reported values. These higher fluxes result from the enhanced measured dissipation rates of on average $\varepsilon = 1.3 \times 10^{-9}$ W kg^{-1}, and maximum $\varepsilon = 2.4 \times 10^{-9}$ W kg^{-1} found over the AW thermocline, compared to on average $\varepsilon = 9.4 \times 10^{-10}$ W kg^{-1}, maximum $\varepsilon = 9.5 \times 10^{-10}$ W kg^{-1}, observed a decade ago (Sirevaag & Fer, 2012). These higher dissipation rates might have been caused by higher vertical shear between the AW layer and the layer above, but unfortunately no current velocity data is available to confirm this hypothesis.

The measurements at the 24 h station were spatially limited, but covered more than one tidal cycle. Tidal phases can affect turbulent mixing in the Laptev Sea region (Lenn et al., 2011), and the instrument repair break
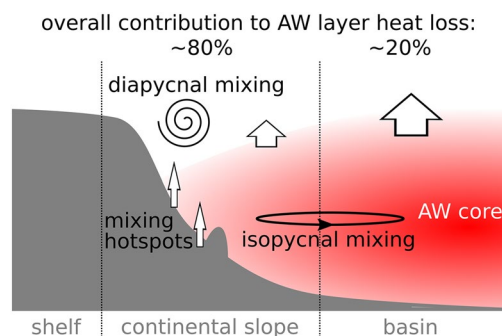
Figure 12. Summary schematic of the summer situation.

might have led to bias in sampling of at least the diurnal tidal period. However, tidal velocities are relatively small in the basin (Baumann et al., 2020), and measured turbulent dissipation rates in the AW thermocline exhibit no distinct trend during the measurement cycle, that could be linked to changes in the tidal phase. We found enhanced heat fluxes in the generally quiescent interior compared with the more dynamic slope region, which contrasts with earlier findings (e.g., Lenn et al., 2009). The large heat flux variability in the AW thermocline above the continental slope (see Table 2) highlights the intermittent nature of turbulence and the limitation of short-term observations. It is likely that episodically enhanced high turbulent mixing, and thus heat flux events, occur in the dynamic continental slope region, probably caused by the interaction of tidal motions with the sloping topography. These processes exhibit dynamics on short time scales that cannot be captured by single-point (in time) observations. This is highlighted by the high dissipation rates found above the continental slope (Figure 3, third profile). The intense vertical mixing at this position led to a weakly stratified to completely mixed water column, and the absence of sharp vertical temperature gradients thus results in very small instantaneous heat fluxes. These instantaneous low heat fluxes do not reflect the strong mixing and the associated high heat fluxes that homogenized the water column prior to the measurements, and do therefore not reflect the importance of slope mixing for the AW heat loss budget.

4.2.2. Boundary Mixing at the Continental Slope

The largest heat fluxes were observed where the warm water of the AW thermocline encountered the cold water of the overlying halocline within the turbulent BBL, and in the BBL at the lee side of a small sill. The application of a constant mixing efficiency in turbulent and weakly stratified environments is strongly debated, and therefore absolute heat flux values should be treated with care as they might overestimate the actual fluxes. However, the identified mixing hotspots are plausible and might be of central importance for the AW heat loss budget, despite their localized appearance.

Data collected during drift stations is always influenced by a combination of spatial and temporal variability, and a discrimination between both is often difficult. The drift track during the 10 h station was clearly influenced by tidal motions (see Figure 10), and tides are known to play an important role in this region (Janout & Lenn, 2014) and influence the near-bottom dynamics in regard to both stratification and mixing (Schulz & Umlauf, 2016; Schulz et al., 2017; Umlauf & Burchard, 2011). Some lines of evidence, however, point to spatial variations as main cause for the observed variability: First, the modeled tidal current as well as the drift did not change direction or speed during the passage of the topographic sill (between 13:00 and 14:00), where high heat fluxes are observed, and second, after the drift and the tidal current changed direction at 19:00, a strongly stratified cold halocline layer and a temperature increase in the near-bottom layer became visible, a vertical structure similar to conditions observed before the turning point of the drift was reached. Still, variability in the observed parameters arising from subtidal variations in the current cannot be excluded or quantified from the available data, but the importance of enhanced mixing in the near-bottom layer in this region is unquestionable.

The importance of boundary mixing was previously emphasized through the use of tracer release experiments in fjords (Stigebrandt, 1979), stratified lakes (Goudsmit et al., 1997), and ocean basins (Holtermann et al., 2012; Ledwell & Bratkovich, 1995). Despite differing setups, the experiments shared similar results. Upon release in the interior region, the tracers first spread laterally (isopycnal mixing) until reaching the sloping boundary where vertical mixing strongly increases (diapycnal mixing), followed by a return of the tracers back into the interior (isopycnal mixing). All studies reported an order of magnitude difference between interior and basin-scale effective diffusivities, and attributed this to the dominance of boundary processes in controlling diapycnal fluxes.

Numerous other studies found boundary processes to be of major importance for basin-scale mixing in continental shelf regions. Factors such as inhomogeneities in stratification (pycnocline layers, fronts) and topography (sills, changes in bottom roughness or slope angle), as well as critical slopes for internal wave

breaking facilitate the exchange between the BBL and interior regions (McPhee-Shaw, 2006, and the references therein). To maintain effective mixing in the bottom boundary layer, some process to restore near-bottom gradients is required, and indeed, the boundary layer over sloping topography was found to be only intermittently well-mixed (McPhee-Shaw, 2006; White, 1994, this study). Candidates for restratifying processes are, among many others, the along-slope advection of stratification with the boundary current, the cross-slope advection of buoyancy anomalies by Ekman transport, on timescales of a few days, (White, 1994, and the references therein), or, on subtidal time scales, an episodic straining of the near-bottom isopycnals induced by the interaction of tidal currents with the sloping topography (Schulz & Umlauf, 2016; Schulz et al., 2017; Umlauf & Burchard, 2011; White, 1994).

The importance of mixing near sloping boundaries has previously been reported in the study region: Lenn et al. (2009) suggested that mixing with cold shelf waters at the continental slope is partly responsible for the observed ABC cooling. Heat flux estimates derived from a vessel-mounted current profiler combined with CTD profiles presented by Dewey et al. (1999) are quantitatively not comparable to the direct heat flux observations presented in this study (due to the different instrumentation and methods), but the authors identified similar mixing hotspots over the western Laptev continental shelf and slope with 5–10 times higher heat fluxes than in deeper regions. Rippeth et al. (2015) found an average (microstructure-derived) heat flux of 22 W m^{-2} across the AW interface between Svalbard and the East Siberian Sea. Their results indicated two orders of magnitude higher fluxes above the slopes than in the central Arctic Ocean, and emphasized the interaction of tides with the sloping bathymetry as the dominant mixing mechanism.

4.2.3. Other Mechanisms

In addition to the heat loss at the upper AW interface and above the continental slope, the presence of straits and canyons, such as Vilkitsky and Shokalsky Straits in the western Laptev Sea, can impact mixing-relevant processes and thus the ABC's heat budget. These straits form potential pathways for cold and dense shelf water from the Kara Sea, and are regions of complex topography that could enhance vertical mixing and trigger the formation of eddies (Janout et al., 2015, 2017). Mooring records from the Laptev Sea slope found eddies to be present 20%–25% of the time, with a three-fold vertical heat flux increase in their vicinity compared to ambient values (Pnyushkov et al., 2018).

The cooling mechanisms presented in this paper were derived from data collected in summer. During freezing season, the mechanisms responsible for AW cooling might be very different. During sea ice formation, another effective mechanism to remove heat from the AW layer is the interaction with near-freezing dense water cascades resulting from brine rejection. When sufficiently dense, these plumes could propagate down the slope and entrain ambient AW (and therefore heat), that is then transported to deeper layers of the Arctic Ocean (Ivanov et al., 2004). As opposed to earlier surveys of the western Laptev Sea (Janout et al., 2017), however, we did not observe any remnants of near-freezing waters dense enough to potentially flow down the continental slope below the AW layer (see Section 3.2).

4.3. AW Mixing in the Future Arctic

A continuing warming in the Arctic may lead to a transition toward further sea ice reduction, weaker stratification and deeper seasonal mixed layers, and an overall wider influence of the AW on the Eurasian slope region (i.e., Atlantification, Polyakov et al., 2017). Recent mooring records indicate a transition toward increased shear and weaker stratification (Polyakov et al., 2020b), and expected consequences include a deeper winter ventilation of AW. While SML and AW heat accumulates in the cold halocline layer in summer (Figure 9 and Table 2), an increased transfer of that heat to the surface occurs in winter. This is due to brine-driven convection during ice formation, and enhanced vertical shear below the SML triggered by winter storms and drifting sea ice. If stratification is weak enough, for instance due to decreasing sea ice melt, winter convection may erode the cold halocline, as was reflected in a 130 m SML near Franz Josef Land in March to April 2014 (Polyakov et al., 2017). However, corresponding measurements further east along the Lomonosov Ridge showed stable cold halocline layers throughout all seasons and no signs of deeper winter ventilation. It hence remains an ongoing question whether deep winter ventilation presently occurs in the

Laptev and East Siberian Seas, but an eastward progressing change of conditions toward a seasonal cold halocline layer is anticipated in the future (Polyakov et al., 2017, 2020a), with considerable consequences for the vertical heat transfer especially in winter.

In a recent model study, Wang et al. (2020) indicate a future acceleration and increase in ABC warming and volume transport, which potentially increases vertical heat fluxes along the ABC pathway: A faster boundary current would enhance vertical shear and hence shear-driven mixing, while a warmer AW layer increases the vertical temperature gradient. The fate of the additional heat remains speculation, a regionally enhanced transfer of AW heat to the ocean surface, and enhanced along-slope heat transport seem plausible. Overall these ongoing changes are expected to significantly impact the pan-Arctic mixing regime.

5. Summary and Conclusions

A comprehensive collection of CTD and microstructure profiles along with two multihour microstructure time series measurements from summer 2018 provides updated insights into the heat budget of the Eurasian continental slope region and into processes leading to cooling of the ABC during its eastward propagation along the Laptev and East Siberian Seas. The mean heat loss of the upper ocean (30–300 m) in this area is found to be $\mathcal{O}(10^8)$ J m^{-2} over 100 km propagation distance. The observed vertical heat flux in the AW thermocline away from the continental slope of approximately 10 W m^{-2} is higher than estimates for this region a decade ago (Lenn et al., 2009; Sirevaag & Fer, 2012), but still only accounts for ~20% of the heat loss required to balance the estimated cooling of 47 W m^{-2} along the boundary current pathway. The largest fraction of the heat loss is thus attributed to mixing with ambient cold water in the continental slope region (Figure 12). There, the observed dissipation rates were highest but heat fluxes (4 W m^{-2}) were lower than in the deep basin, which is due to weaker temperature gradients as a result of the enhanced mixing. Heat fluxes were strongly elevated in the near-bottom region above the slope, where deep warm water intersects the turbulent bottom boundary layer, as well as on the lee side of a topographic sill, as was observed during a 10 h-microstructure survey from a freely drifting ship. Our observations indicate that diapycnal mixing prevails above the slope, while the basin regions are dominated by lateral homogenization of the AW layer through isopycnal mixing (Figure 12), which agrees with the general perception that basin-wide diapycnal mixing is to first order determined by boundary mixing, while lateral (isopycnal) mixing dominates the calmer interior regions (Goudsmit et al., 1997; Holtermann et al., 2012; Ledwell & Bratkovich, 1995; Stigebrandt, 1979). Other processes such as winter ventilation that could potentially contribute to AW heat loss, are unlikely to play a dominant role in the present eastern Eurasian Arctic, although long-term mooring records indicate transitions toward weaker stratification and stronger shear-driven mixing (Polyakov et al., 2020b), which could ultimately lead to the disappearance of the cold halocline (Polyakov et al., 2020a) and thus a direct impact of AW heat on the Arctic ice cover.

Further investigations of boundary layer processes along the continental shelf are needed to fully understand the dispersal of AW heat along the boundary current pathway. The interaction of tidal currents with sloping topography and restratification mechanisms in the bottom boundary layer, as well as the exchange between bottom boundary layer and interior regions are poorly understood and require more attention. Further, the effect of topographic irregularities such as sills on the heat budget requires detailed studies, as these are often too small to be resolved in bathymetric data products and ocean models. Arctic continental slopes generally feature productive ecosystems (Bluhm et al., 2020), which are supported and maintained by complex ocean dynamics including boundary layer mixing and enhanced vertical nutrient fluxes (Randelhoff et al., 2020). The episodic nature of turbulence is a major source of uncertainty for heat budgets as well as for nutrient fluxes, and therefore requires enhanced efforts to develop and improve mooring-based methods to measure turbulent mixing year-round.

Data Availability Statement

Hydrographic data used in this study is available at: https://doi.pangaea.de/10.1594/PANGAEA.902600 (UCTD). Igor Polyakov. 2019. Acoustic Doppler current profiler (ADCP) from moorings taken in the Eurasian and Makarov Basins, Arctic Ocean, 2015–2018. Arctic Data Center. https://doi.org/10.18739/A2HT2GB80,

References

Aagaard, K., Foldvik, A., & Hillman, S. (1987). The West Spitsbergen Current: Disposition and water mass transformation. *Journal of Geophysical Research*, *92*(C4), 3778–3784.

Årthun, M., Eldevik, T., Smedsrud, L., Skagseth, Ø., & Ingvaldsen, R. (2012). Quantifying the influence of Atlantic heat on Barents Sea ice variability and retreat. *Journal of Climate*, *25*(13), 4736–4743. https://doi.org/10.1175/JCLI-D-11-00466.1

Baumann, T. M., Polyakov, I. V., Padman, L., Danielson, S., Fer, I., Janout, M., et al. (2020). Arctic tidal current atlas. *Scientific Data*, *7*(1), 1–11. https://doi.org/10.1038/s41597-020-00578-z

Baumann, T. M., Polyakov, I. V., Pnyushkov, A. V., Rember, R., Ivanov, V. V., Alkire, M. B., et al. (2018). On the seasonal cycles observed at the continental slope of the Eastern Eurasian Basin of the Arctic Ocean. *Journal of Physical Oceanography*, *48*(7), 1451–1470. https://doi.org/10.1175/JPO-D-17-0163.1

Becherer, J., Stacey, M. T., Umlauf, L., & Burchard, H. (2015). Lateral circulation generates flood tide stratification and estuarine exchange flow in a curved tidal inlet. *Journal of Physical Oceanography*, *45*(3), 638–656. https://doi.org/10.1175/JPO-D-14-0001.1

Beszczynska-Möller, A., Fahrbach, E., Schauer, U., & Hansen, E. (2012). Variability in Atlantic water temperature and transport at the entrance to the Arctic Ocean, 1997–2010. *ICES Journal of Marine Science*, *69*(5), 852–863. https://doi.org/10.1093/icesjms/fss056

Bluhm, B., Janout, M., Danielson, S., Ellingsen, I., Gavrilo, M., Grebmeier, J., et al. (2020). The pan-Arctic continental slope: A narrow band of strong physical gradients affecting pelagic and benthic ecosystems. *Frontiers in Marine Science*, *7*, 544386.

Boitsov, V. D., Karsakov, A. L., & Trofimov, A. G. (2012). Atlantic water temperature and climate in the Barents Sea, 2000–2009. *ICES Journal of Marine Science*, *69*(5), 833–840. https://doi.org/10.1093/icesjms/fss075

Bourgain, P., & Gascard, J.-C. (2011). The Arctic Ocean halocline and its interannual variability from 1997 to 2008. *Deep Sea Research Part I: Oceanographic Research Papers*, *58*(7), 745–756. https://doi.org/10.1016/j.dsr.2011.05.001

Coachman, L., & Barnes, C. (1963). The movement of Atlantic water in the Arctic Ocean. *Arctic*, *16*(1), 8–16.

Dewey, R., Muench, R., & Gunn, J. (1999). Mixing and vertical heat flux estimates in the Arctic Eurasian Basin. *Journal of Marine Systems*, *21*(1–4), 199–205.

Dmitrenko, I. A., Polyakov, I. V., Kirillov, S. A., Timokhov, L. A., Frolov, I. E., Sokolov, V. T., et al. (2008). Toward a warmer Arctic Ocean: Spreading of the early 21st century Atlantic Water warm anomaly along the Eurasian Basin margins. *Journal of Geophysical Research*, *113*(C5). https://doi.org/10.1029/2007JC004158

Fer, I. (2009). Weak vertical diffusion allows maintenance of cold halocline in the central Arctic. *Atmospheric and Oceanic Science Letters*, *2*(3), 148–152. https://doi.org/10.1080/16742834.2009.11446789

Fer, I., Koenig, Z., Kozlov, I. E., Ostrowski, M., Rippeth, T. P., Padman, L., et al. (2020). Tidally Forced Lee Waves Drive Turbulent Mixing Along the Arctic Ocean Margins. *Geophysical Research Letters*, *47*(16), e2020GL088083. https://doi.org/10.1029/2020GL088083

Goudsmit, G.-H., Peeters, F., Gloor, M., & Wüest, A. (1997). Boundary versus internal diapycnal mixing in stratified natural waters. *Journal of Geophysical Research*, *102*(C13), 27903–27914.

Gregg, M., D'Asaro, E., Riley, J., & Kunze, E. (2018). Mixing efficiency in the ocean. *Annual Review of Marine Science*, *10*, 443–473. https://doi.org/10.1146/annurev-marine-121916-063643

Guthrie, J. D., Fer, I., & Morison, J. H. (2017). Thermohaline staircases in the Amundsen Basin: Possible disruption by shear and mixing. *Journal of Geophysical Research: Oceans*, *122*(10), 7767–7782. https://doi.org/10.1002/2017JC012993

Holtermann, P. L., Umlauf, L., Tanhua, T., Schmale, O., Rehder, G., & Waniek, J. J. (2012). The Baltic Sea tracer release experiment: 1. Mixing rates. *Journal of Geophysical Research: Oceans*, *117*(C1). https://doi.org/10.1029/2011JC007439

Inoue, R., Yamazaki, H., Wolk, F., Kono, T., & Yoshida, J. (2007). An estimation of buoyancy flux for a mixture of turbulence and double diffusion. *Journal of Physical Oceanography*, *37*(3), 611–624. https://doi.org/10.1175/JPO2996.1

Ivanov, V., Shapiro, G., Huthnance, J., Aleynik, D., & Golovin, P. (2004). Cascades of dense water around the world ocean. *Progress in Oceanography*, *60*(1), 47–98. https://doi.org/10.1016/j.pocean.2003.12.002

Jakobsson, M., Mayer, L., Coakley, B., Dowdeswell, J. A., Forbes, S., Fridman, B., et al. (2012). The International Bathymetric Chart of the Arctic Ocean (IBCAO) version 3.0. *Geophysical Research Letters*, *39*(12). https://doi.org/10.1029/2012GL052219

Janout, M. A., Aksenov, Y., Hölemann, J. A., Rabe, B., Schauer, U., Polyakov, I. V., et al. (2015). Kara Sea freshwater transport through Vilkitsky Strait: Variability, forcing, and further pathways toward the western Arctic Ocean from a model and observations. *Journal of Geophysical Research: Oceans*, *120*(7), 4925–4944. https://doi.org/10.1002/2014JC010635

Janout, M. A., Hölemann, J., Timokhov, L., Gutjahr, O., & Heinemann, G. (2017). Circulation in the northwest Laptev Sea in the eastern Arctic Ocean: Crossroads between Siberian River water, Atlantic water and polynya-formed dense water. *Journal of Geophysical Research: Oceans*, *122*(8), 6630–6647. https://doi.org/10.1002/2017JC013159

Janout, M. A., & Lenn, Y.-D. (2014). Semidiurnal tides on the Laptev Sea shelf with implications for shear and vertical mixing. *Journal of Physical Oceanography*, *44*(1), 202–219. https://doi.org/10.1175/JPO-D-12-0240.1

Kelley, D. E. (1990). Fluxes through diffusive staircases: A new formulation. *Journal of Geophysical Research*, *95*(C3), 3365–3371.

Ledwell, J. R., & Bratkovich, A. (1995). A tracer study of mixing in the Santa Cruz Basin. *Journal of Geophysical Research*, *100*(C10), 20681–20704.

Lee, C., Chang, K.-I., Lee, J. H., & Richards, K. J. (2014). Vertical mixing due to double diffusion in the tropical western Pacific. *Geophysical Research Letters*, *41*(22), 7964–7970. https://doi.org/10.1002/2014GL061698

Lenn, Y.-D., Rippeth, T. P., Old, C. P., Bacon, S., Polyakov, I., Ivanov, V., & Hölemann, J. (2011). Intermittent intense turbulent mixing under ice in the Laptev Sea continental shelf. *Journal of Physical Oceanography*, *41*(3), 531–547. https://doi.org/10.1175/2010JPO4425.1

Lenn, Y.-D., Wiles, P., Torres-Valdes, S., Abrahamsen, E., Rippeth, T., Simpson, J., et al. (2009). Vertical mixing at intermediate depths in the Arctic boundary current. *Geophysical Research Letters*, *36*(5). https://doi.org/10.1029/2008GL036792

McDougall, T. J., & Barker, P. M. (2011). Getting started with TEOS-10 and the Gibbs Seawater (GSW) oceanographic toolbox. *SCOR/IAPSO WG*, *127*, 1–28.

McPhee-Shaw, E. (2006). Boundary–interior exchange: Reviewing the idea that internal-wave mixing enhances lateral dispersal near continental margins. *Deep Sea Research Part II: Topical Studies in Oceanography*, *53*(1–2), 42–59. https://doi.org/10.1016/j.dsr2.2005.10.018

Meyer, A., Fer, I., Sundfjord, A., & Peterson, A. K. (2017). Mixing rates and vertical heat fluxes north of Svalbard from Arctic winter to spring. *Journal of Geophysical Research: Oceans*, *122*(6), 4569–4586. https://doi.org/10.1002/2016JC012441

Nakano, H., & Yoshida, J. (2019). A note on estimating eddy diffusivity for oceanic double-diffusive convection. *Journal of Oceanography*, *75*, 375–393. https://doi.org/10.1007/s10872-019-00514-9

Nansen, F. (1902). The oceanography of the North Polar basin. The Norwegian North Polar Expedition 1893–1896. Scientific Results (Vol. 9, No. 3, p. 427). New York, NY: Greenwood Press.

Nasmyth, P. W. (1970). *Oceanic turbulence* (Unpublished doctoral dissertation). University of British Columbia. https://doi.org/10.14288/1.0302459

Osborn, T. (1980). Estimates of the local rate of vertical diffusion from dissipation measurements. *Journal of Physical Oceanography*, *10*(1), 83–89.

Padman, L. (1994). Momentum fluxes through sheared oceanic thermohaline steps. *Journal of Geophysical Research*, *99*(C11), 22491–22499.

Padman, L., & Erofeeva, S. (2004). A barotropic inverse tidal model for the Arctic Ocean. *Geophysical Research Letters*, *31*(2). https://doi.org/10.1029/2003GL019003

Panteleev, G., Proshutinsky, A., Kulakov, M., Nechaev, D. A., & Maslowski, W. (2007). Investigation of the summer Kara Sea circulation employing a variational data assimilation technique. *Journal of Geophysical Research*, *112*(C4). https://doi.org/10.1029/2006JC003728

Pawlowicz, R. (2000). *M_Map: A mapping package for Matlab*. University of British Columbia Earth and Ocean Sciences. Retrieved from http://www.eos.ubc.ca/rich/map.html

Pnyushkov, A. V., Polyakov, I. V., Ivanov, V. V., Aksenov, Y., Coward, A. C., Janout, M., & Rabe, B. (2015). Structure and variability of the boundary current in the Eurasian Basin of the Arctic Ocean. *Deep Sea Research Part I: Oceanographic Research Papers*, *101*, 80–97. https://doi.org/10.1016/j.dsr.2015.03.001

Pnyushkov, A. V., Polyakov, I. V., Ivanov, V. V., & Kikuchi, T. (2013). Structure of the Fram Strait branch of the boundary current in the Eurasian Basin of the Arctic Ocean. *Polar Science*, *7*(2), 53–71. https://doi.org/10.1016/j.polar.2013.02.001

Pnyushkov, A. V., Polyakov, I. V., Padman, L., & Nguyen, A. T. (2018). Structure and dynamics of mesoscale eddies over the Laptev Sea continental slope in the Arctic Ocean. *Ocean Science*, *14*(5), 1329–1347. https://doi.org/10.5194/os-14-1329-2018

Polyakov, I. V., Padman, L., Lenn, Y.-D., Pnyushkov, A., Rember, R., & Ivanov, V. V. (2019). Eastern Arctic Ocean diapycnal heat fluxes through large double-diffusive steps. *Journal of Physical Oceanography*, *49*(1), 227–246. https://doi.org/10.1175/JPO-D-18-0080.1

Polyakov, I. V., Pnyushkov, A. V., Alkire, M. B., Ashik, I. M., Baumann, T. M., Carmack, E. C., et al. (2017). Greater role for Atlantic inflows on sea-ice loss in the Eurasian Basin of the Arctic Ocean. *Science*, *356*(6335), 285–291. https://doi.org/10.1126/science.aai8204

Polyakov, I. V., Rippeth, T. P., Fer, I., Alkire, M. B., Baumann, T. M., Carmack, E. C., et al. (2020a). Weakening of cold halocline layer exposes sea ice to oceanic heat in the eastern Arctic Ocean. *Journal of Climate*, *33*(18), 8107–8123. https://doi.org/10.1175/JCLI-D-19-0976.1

Polyakov, I. V., Rippeth, T. P., Fer, I., Baumann, T. M., Carmack, E. C., Ivanov, V. V., et al. (2020b). Intensification of Near-Surface Currents and Shear in the Eastern Arctic Ocean. *Geophysical Research Letters*, *47*(16), e2020GL089469. https://doi.org/10.1029/2020GL089469

Polyakov, I. V., Timokhov, L. A., Alexeev, V. A., Bacon, S., Dmitrenko, I. A., Fortier, L., et al. (2010). Arctic Ocean warming contributes to reduced polar ice cap. *Journal of Physical Oceanography*, *40*(12), 2743–2756. https://doi.org/10.1175/2010JPO4339.1

Rainville, L., & Winsor, P. (2008). Mixing across the Arctic Ocean: Microstructure observations during the Beringia 2005 expedition. *Geophysical Research Letters*, *35*(8). https://doi.org/10.1029/2008GL033532

Randelhoff, A., Holding, J., Janout, M., Sejr, M. K., Babin, M., Tremblay, J.-É., & Alkire, M. B. (2020). Pan-Arctic Ocean primary production constrained by turbulent nitrate fluxes. *Frontiers in Marine Science*, *7*(150). https://doi.org/10.3389/fmars.2020.00150

Renner, A., Sundfjord, A., Janout, M., Ingvaldsen, R. B., Beszczynska-Möller, A., Pickart, R. S., & Pérez-Hernández, M. D. (2018). Variability and redistribution of heat in the Atlantic water boundary current north of Svalbard. *Journal of Geophysical Research: Oceans*, *123*(9), 6373–6391. https://doi.org/10.1029/2018JC013814

Rippeth, T. P., Lincoln, B. J., Lenn, Y.-D., Green, J. M., Sundfjord, A., & Bacon, S. (2015). Tide-mediated warming of Arctic halocline by Atlantic heat fluxes over rough topography. *Nature Geoscience*, *8*(3), 191–194. https://doi.org/10.1038/ngeo2350

Rudels, B. (2012). Arctic Ocean circulation and variability-advection and external forcing encounter constraints and local processes. *Ocean Science*, *8*, 261–286. https://doi.org/10.5194/os-8-261-2012

Rudels, B., Meyer, R., Fahrbach, E., Ivanov, V., Østerhus, S., Quadfasel, D., et al. (2000). Water mass distribution in Fram Strait and over the Yermak Plateau in summer 1997. Annales geophysicae (Vol. 18, pp. 687–705. https://doi.org/10.1007/s00585-000-0687-5

Schauer, U., Muench, R. D., Rudels, B., & Timokhov, L. (1997). Impact of eastern Arctic shelf waters on the Nansen Basin intermediate layers. *Journal of Geophysical Research*, *102*(C2), 3371–3382. https://doi.org/10.1002/2016JC012448

Schulz, K., Endoh, T., & Umlauf, L. (2017). Slope-induced tidal straining: Analysis of rotational effects. *Journal of Geophysical Research: Oceans*, *122*(3), 2069–2089. https://doi.org/10.1002/2016JC012448

Schulz, K., & Umlauf, L. (2016). Residual transport of suspended material by tidal straining near sloping topography. *Journal of Physical Oceanography*, *46*(7), 2083–2102. https://doi.org/10.1175/JPO-D-15-0218.1

Scotti, A., & White, B. (2016). The mixing efficiency of stratified turbulent boundary layers. *Journal of Physical Oceanography*, *46*(10), 3181–3191. https://doi.org/10.1175/JPO-D-16-0095.1

Shibley, N. C., Timmermans, M.-L., Carpenter, J. R., & Toole, J. M. (2017). Spatial variability of the Arctic Ocean's double-diffusive staircase. *Journal of Geophysical Research: Oceans*, *122*(2), 980–994. https://doi.org/10.1002/2016JC012419

Shih, L. H., Koseff, J. R., Ivey, G. N., & Ferziger, J. H. (2005). Parameterization of turbulent fluxes and scales using homogeneous sheared stably stratified turbulence simulations. *Journal of Fluid Mechanics*, *525*, 193–214. https://doi.org/10.1017/S002211200400258

Sirevaag, A., & Fer, I. (2012). Vertical heat transfer in the Arctic Ocean: The role of double-diffusive mixing. *Journal of Geophysical Research: Oceans*, *117*(C7). https://doi.org/10.1029/2012JC007910

Slinn, D. N., & Riley, J. J. (1996). Turbulent mixing in the oceanic boundary layer caused by internal wave reflection from sloping terrain. *Dynamics of Atmospheres and Oceans*, *24*(1–4), 51–62.

Smedsrud, L. H., Esau, I., Ingvaldsen, R. B., Eldevik, T., Haugan, P. M., Li, C., et al. (2013). The role of the Barents Sea in the Arctic climate system. *Reviews of Geophysics*, *51*(3), 415–449. https://doi.org/10.1002/rog.20017

Stigebrandt, A. (1979). Observational evidence for vertical diffusion driven by internal waves of tidal origin in the Oslofjord. *Journal of Physical Oceanography*, *9*(2), 435–441.

St. Laurent, L., & Schmitt, R. W. (1999). The contribution of salt fingers to vertical mixing in the North Atlantic Tracer Release Experiment. *Journal of Physical Oceanography*, *29*(7), 1404–1424.

Tarasenko, A., Supply, A., Kusse-Tiuz, N., Ivanov, V., Makhotin, M., Tournadre, J., et al. (2019). Surface waters properties in the Laptev and the East-Siberian Seas in summer 2018 from in situ and satellite data. *Ocean Science Discussions*.

Thyng, K. M., Greene, C. A., Hetland, R. D., Zimmerle, H. M., & DiMarco, S. F. (2016). True colors of oceanography: Guidelines for effective and accurate colormap selection. *Oceanography*, *29*(3), 9–13. Retrieved from http://www.jstor.org/stable/24862699

Turner, J. S. (2010). The melting of ice in the Arctic Ocean: The influence of double-diffusive transport of heat from below. *Journal of Physical Oceanography*, *40*(1), 249–256. https://doi.org/10.1175/2009JPO4279.1

Umlauf, L., & Burchard, H. (2011). Diapycnal transport and mixing efficiency in stratified boundary layers near sloping topography. *Journal of Physical Oceanography*, *41*(2), 329–345. https://doi.org/10.1175/2010JPO4438.1

Walsh, D., Polyakov, I., Timokhov, L., & Carmack, E. (2007). Thermohaline structure and variability in the eastern Nansen Basin as seen from historical data. *Journal of Marine Research*, *65*(5), 685–714. https://doi.org/10.1357/002224007783649466

Wang, Q., Wekerle, C., Wang, X., Danilov, S., Koldunov, N., Sein, D., et al. (2020). Intensification of the Atlantic Water supply to the Arctic Ocean through Fram Strait induced by Arctic sea ice decline. *Geophysical Research Letters*, *47*(3), e2019GL086682. https://doi.org/10.1029/2019GL086682

White, M. (1994). Tidal and subtidal variability in the sloping benthic boundary layer. *Journal of Geophysical Research*, *99*(C4), 7851–7864.

Woodgate, R. A., Aagaard, K., Muench, R. D., Gunn, J., Björk, G., Rudels, B., et al. (2001). The Arctic Ocean boundary current along the Eurasian slope and the adjacent Lomonosov Ridge: Water mass properties, transports and transformations from moored instruments. *Deep Sea Research Part I: Oceanographic Research Papers*, *48*(8), 1757–1792.

Zhurbas, N., & Kuzmina, N. (2020). Variability of the thermohaline structure and transport of Atlantic water in the Arctic Ocean based on NABOS (Nansen and Amundsen Basins Observing System) hydrography data. *Ocean Science*, *16*(2), 405–421. https://doi.org/10.5194/os-16-405-2020